

Proximal lava drainage controls on basaltic fissure eruption dynamics

T. J. Jones¹ · E. W. Llewellyn¹ · B. F. Houghton² · R. J. Brown¹ · C. Vye-Brown³

Received: 10 June 2017 / Accepted: 3 October 2017
© The Author(s) 2017. This article is an open access publication

Abstract Hawaiian basaltic eruptions commonly initiate as a fissure, producing fountains, spattering, and clastogenic lava flows. Most fissures rapidly localize to form a small number of eruptive vents, the location of which may influence the subsequent distribution of lava flows and associated hazards. We present results from a detailed field investigation of the proximal deposits of episode 1 of the 1969 fissure eruption of Mauna Ulu, Kīlauea, Hawai‘i. Exceptional preservation of the deposits allows us to reconstruct vent-proximal lava drainage patterns and to assess the role that drainage played in constraining vent localization. Through detailed field mapping, including measurements of the height and internal depth of lava tree moulds, we reconstruct high-resolution topographic maps of the pre-eruption ground surface, the lava high-stand surface and the post-eruption ground surface. We calculate the difference in elevation between pairs of maps to estimate the lava inundation depth and lava drainage depth over the field area and along different segments of fissure. Aerial photographs collected during episode 1 of the eruption allow us to locate those parts of the fissure that are no longer

exposed at the surface. By comparing with the inundation and drainage maps, we find that fissure segments that were inundated with lava to greater depths (typically 1–6 m) during the eruption later became foci of lava drainage back into the fissure (internal drain-back). We infer that, in these areas, lava ponding over the fissure suppressed discharge of magma, thereby favouring drain-back and stagnation. By contrast, segments with relatively shallow inundation (typically less than ~1 m), such as where the fissure intersects pre-eruptive topographic highs, or where flow away from the vent (outflow) was efficient, are often associated with sub-circular vent geometries in the post-eruption ground surface. We infer that these parts of the fissure became localization points for ongoing magma ascent and discharge. We conclude that lava inundation and drainage processes in basaltic fissure eruptions can play an important role in controlling their localization and longevity.

Keywords Mauna Ulu · Vent localization · Lava ponding · Lava tree moulds · Eruption longevity · Vent inundation

Editorial responsibility: J. Taddeucci

Electronic supplementary material The online version of this article (<https://doi.org/10.1007/s00445-017-1164-2>) contains supplementary material, which is available to authorized users.

✉ T. J. Jones
t.j.jones@durham.ac.uk

¹ Department of Earth Sciences, Durham University, South Road, Durham DH1 3LE, UK

² Department of Geology & Geophysics, SOEST, University of Hawai‘i at Mānoa, Honolulu, HI 96822, USA

³ British Geological Survey, The Lyell Centre, Research Avenue South, Edinburgh EH14 4AP, UK

Introduction

Basaltic fissure eruptions account for the bulk of the Earth’s magma output (Sigurdsson 2000). Although relatively common, their deposits can nonetheless be challenging to investigate and interpret. Vent structures are known to evolve and migrate during eruptions (e.g. Richter et al. 1970; Thorarinnsson et al. 1973; Swanson et al. 1979; Bruce and Huppert 1989); however, evidence of these dynamic processes is commonly buried beneath later syn-eruptive material, including spatter, tephra fall and subsequent lava flows (e.g. Thordarson and Self 1993; Larsen 2000; Brown et al. 2015; Reynolds et al. 2016). Furthermore, evidence of clastogenic

eruption processes, such as spattering and fountaining, can be lost if pyroclastic material becomes agglutinated and/or forms rheomorphic lava flows (Sumner et al. 2005; Valentine and Gregg 2008; Parcheta et al. 2012).

Basaltic fissure eruptions typically initiate as curtains of fountaining basaltic spatter, bombs and lapilli, with heights of 10s to 100s of meters (e.g. Richter et al. 1970; Swanson et al. 1979; Wolfe 1988; Alparone et al. 2003). The vents are initially of high aspect ratio, with crack widths varying from ~ 2 m to tens of meters and lengths ranging from several hundred metres to several kilometres (e.g. Gudmundsson 1987; Opheim and Gudmundsson 1989; Keating et al. 2008; Parcheta et al. 2015). Over the order of hours, the curtain generally focuses to a few point sources along the fissure (e.g. Richter et al. 1970; Thorarinsson et al. 1973; Swanson et al. 1979); however, controls on the temporal and spatial evolution of such systems are poorly understood (Bruce and Huppert 1989). Progressive localization causes a change in the eruption parameters, such as an increase in fountain height (Wilson et al. 1995), restricted spatial distributions of lava discharge (Pedersen et al. 2017) and release of hazardous gases and aerosols (Walker et al. 1984; Stothers et al. 1986; Woods 1993) from a point, rather than a line, source. To track, and thus effectively manage, this dynamic situation, a better understanding of factors modulating fissure localization is required.

Previous studies of vent localization and termination of basaltic fissure eruptions have focused on thermo-rheological effects and the solidification of magma in the feeder dyke. Delaney and Pollard (1982) calculated that magma flowing at 1 m s^{-1} in a 2-m-wide dyke should rapidly cool and solidify inwards from conduit margins to close the dyke within a few hours. They inferred that, for eruptions to last longer than a few hours, as observed in Iceland (Thorarinsson et al. 1973) and Hawai'i (Swanson et al. 1979), the width of the ascending dyke must be greater than 2 m. Bruce and Huppert (1989) investigated the role of thermo-rheological effects in vent-localization. They showed that the balance between heat transfer by advection and conduction governs whether conduit walls are melted back, widening the conduit, or magma solidifies against the walls, narrowing and eventually blocking the conduit (Bruce and Huppert 1989; Bruce and Huppert 1990). More recent work has shown that, as the magma cools against the wall rock, local regions of relatively cooler, and higher viscosity magma are formed (Wylie and Lister 1995; Wylie et al. 1999). The fresh, hotter upwelling magma will tend to minimize energy loss by flowing through the regions of lowest viscosity, forming fingers of localized upwelling (Whitehead and Helfrich 1991; Helfrich 1995; Wylie and Lister 1995; Wylie et al. 1999).

Flow organization within basaltic feeder systems must also be influenced by drain-back of dense, degassed magma into the conduit. Drain-back has been documented at several lava

lakes, such as at Halema'uma'u Crater, Kīlauea Iki and Makaopuhi on Kīlauea, Hawai'i (Wright et al. 1968; Richter et al. 1970; Swanson et al. 1979; Stovall et al. 2009; Patrick et al. 2015), Mt. Erebus, Antarctica (e.g. Oppenheimer and Kyle 2008) and Erta Ale, Ethiopia (Oppenheimer and Francis 1997). At these systems, fluctuations in the height of a lava lake have been related to pressure changes, magma flux or gas flux within the magma plumbing system (e.g. Tilling 1987; Witham and Llewellyn 2006; Patrick et al. 2015). Bidirectional flow induced by the descent of relatively degassed, dense magma in a conduit has been investigated for the case of a vertical, cylindrical conduit geometry, and the upwelling and downwelling components organized either as core-annular flow or side-by-side flow, depending on the viscosity ratio (Kazahaya et al. 1994; Stevenson and Blake 1998; Huppert and Hallworth 2007; Beckett et al. 2011; Palma et al. 2011; Beckett et al. 2014). Bidirectional flow has also been inferred from mass balance calculations at lava lakes; that is, to maintain a non-overflowing lake, supply into the lake must be balanced by flow back down the conduit (Tilling 1987; Harris et al. 1999; Witham and Llewellyn 2006; Harris 2008).

In some cases, lava has been directly observed to drain back down a fissure system, such as the 2002 eruption of Nyiragongo (Allard et al. 2002; Wunderman 2002), 1974 eruption of Kīlauea (Tilling et al. 1987; Wilson et al. 1995) and the 2011 Kamoamoā eruption (Orr et al. 2015). Drainage has also been inferred from studies of exposed vent deposits and dyke feeder systems at a range of depths (Lefebvre et al. 2012; Geshi and Neri 2014; Wadsworth et al. 2015). At greater depths, regions of both upwards and downwards flow have been identified within a single camptonite dyke at Higby Mountain, Connecticut (Philpotts and Philpotts 2007).

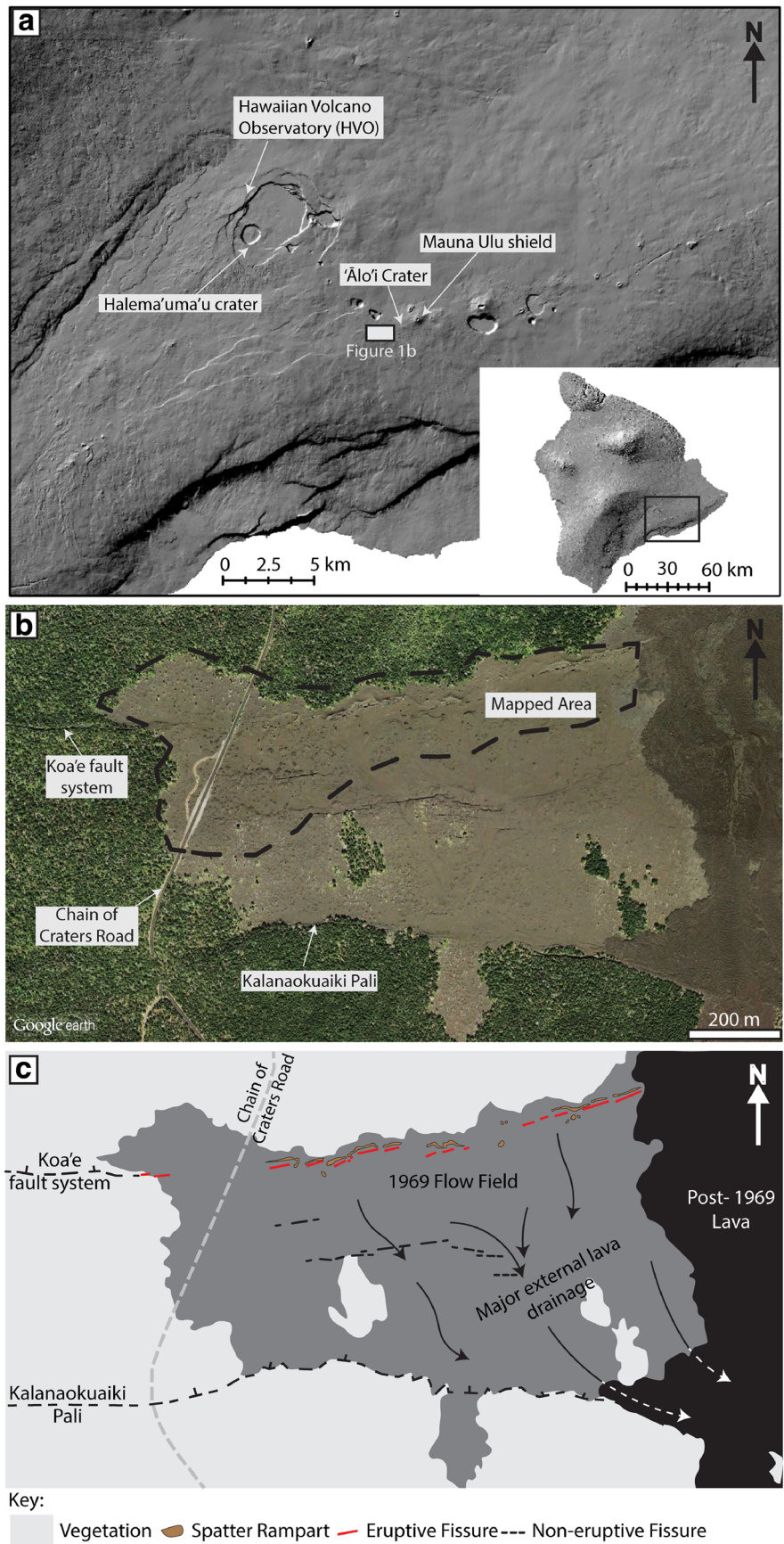
The role that drain-back plays in the evolution of magma flow organization within, and out of, a dyke is currently an open research question. Here, we use field evidence to investigate the inundation and drainage of basaltic lava during episode 1 of the 1969–1974 eruption of Mauna Ulu, Hawai'i, USA, and assess its influence on shallow conduit dynamics and the spatio-temporal evolution of the fissure system.

Background

The Mauna Ulu 1969–1974 eruption

Mauna Ulu is a small lava shield, located on the East Rift Zone (ERZ) of Kīlauea volcano, Hawai'i (Fig. 1a). The 1969–1974 Mauna Ulu eruption that built this shield was characterized by two phases: Phase I began on May 24, 1969 and ended on October 15, 1971 during which $185 \times 10^6 \text{ m}^3$ of lava were erupted (Swanson et al. 1979), and phase II lasted from February 3, 1972 to July 22, 1974 (Tilling et al. 1987). The

Fig. 1 Location map of Mauna Ulu on the Island of Hawai'i. **a** The location of the field area is shown in the black box. **b** Google Earth™ aerial image of the Mauna Ulu lava field; for reference, the centre of the view is at 19° 21' 39.43" N, 155° 13' 5.68" W. **c** Interpreted diagram of the image in **b** showing the surface features of the episode 1 Mauna Ulu eruption



two phases were documented by Swanson et al. (1979) and Tilling et al. (1987), respectively. Here, we follow the narrative of Swanson et al. (1979) and enhanced timings of (Parcheta et al. 2012). Episode 1 of the eruption initiated on May 24, 1969 with an earthquake swarm that could be felt in the nearby village of Volcano. At 04:45 Hawaiian Standard Time (HST), fountaining began from a newly formed fissure system close to ‘Ālo‘i Crater. This fissure rapidly propagated westwards, crossing the old Chain of Craters Road by 05:00 HST, and ‘Āinahou Road (the current Chain of Craters Road; Fig. 1) at 08:30 HST, beyond which it exploited the Koa‘e fault system and terminated ~ 150 m west of ‘Āinahou Road. Steady fountaining and lava ponding occurred until 12:00–13:00 HST. During this time, a pāhoehoe lava field advanced southward down slope from the fissure and ponded 1.2 km from the vent at the base of the north-facing Kalanaokuaiki Pali fault scarp (Fig. 1). Steady fountaining was followed by a period of waning activity and lava drain-back ending at 22:00 HST. This marked the end of episode 1 and the last eruptive activity in the western segment of the Mauna Ulu fissure system. All subsequent activity occurred further to the east, forming the Mauna Ulu shield and its associated lava flow field. Most significantly for this study, a voluminous lava flow in January–March 1974, originating from the Mauna Ulu shield, covered large sections of the originally 4.5-km-long fissure, leaving only the 880 m long western section exposed and available to study today (Fig. 1b, c). Therefore, this study solely focuses on the early development of the fissure system rather than the later phases that were confined to the Mauna Ulu shield to the east; all discussions of lava re-surfacing refer to the 1969 episode 1 eruption. Contemporary observation of episode 1 was limited to eyewitness accounts by Hawaiian Volcano Observatory (HVO) scientists (Swanson et al. 1979) and aerial photographs were taken serendipitously by a Sandia Labs aerial survey (now held at the US Geological Survey HVO; Fig. S1) taken 1 h after the fissure system reached its full length (Swanson et al. 1979; Parcheta et al. 2012).

Previous mapping of the episode 1 fissure system

The exceptional preservation of the episode 1 fissure system offers a unique opportunity to investigate shallow conduit geometries and processes. Parcheta et al. (2015) used ground-based light detection and ranging (LiDAR) to measure the geometry of parts of the shallow conduit (< 15 m depth) and vents associated with the episode 1 fissure system. They mapped 54 vents or fissure segments along the surviving 880 m of fissure and document several distinct geometric features including (1) five en echelon steps caused by the rotation of a rectilinear dyke to a near-shear stress orientation upon ascent; (2) sinuous individual fissure segments most likely related to stress field interactions between the ERZ and the Koa‘e fault system, as well as fissure irregularity; and (3)

irregularity in the internal dyke wall surface, thought to represent pre-existing cooling joints within the pre-1969 lava flow through which the dyke cuts (Parcheta et al. 2015). Three-dimensional imaging of the sub-surface vent structures showed that the primary conduit wall consists of jigsaw-like fits between either side of the conduit (Parcheta et al. 2016), indicating that the conduit walls have not been modified since the eruption.

The vent geometries range from sub-circular to linear in plan view and from parallel-sided to flared in cross-section. The degree of vent flaring was characterized quantitatively through the LiDAR point cloud for three vents (Parcheta et al. 2015). No clear relationship between fountain height and vent flaring was found, although fountain height during the eruption was poorly quantified. Parcheta et al. (2015) suggested that the flaring was caused by either syn-eruptive erosion or late-stage drain-back of ponded lava.

Methods

Fieldwork

In this study, we focus on the near-fissure products of the episode 1 flow field (Fig. 1c). At the time of the eruption, this area was densely forested, and the episode 1 lava flows quenched against the trees. As the flows inflated, the quench surface extended higher up the trees, forming casts up to 5 m high; this lava high-stand surface represents the maximum local inundation depth (Parcheta et al. 2015). During the waning stage of the eruption, lava drained to leave solidified lava quenched against the tree to form a tree mould (Finch 1931; Moore and Richter 1962; Lockwood and Williams 1978; Lockwood and Lipman 1980). The difference in height between the lava high-stand surface and final, post-eruption ground surface represents the extent of drainage from the maximum inundation depth, termed the lava drainage depth (Finch 1931; Moore and Richter 1962; Lockwood and Williams 1978; Parcheta et al. 2015). The entire area was densely forested; hence, tree moulds provide a consistent dataset for inundation depth across the proximal lava flow field fed by the episode 1 fissure.

Measurements of elevation of the lava high-stand (syn-eruption) surface and post-eruption ground surface (i.e. the present day surface) were taken using a Leica SR520 kinematic GPS (kGPS) on > 200 tree moulds (Fig. 2). The following measurements were made for each tree mould, where possible: (1) internal depth of the tree mould (by lowering a plumb-bob into the mould), (2) elevation of the uppermost crust level (lava high-stand), (3) elevation of the post-eruption ground surface around the tree mould (i.e. the level of the surface following drainage) and (4) height of the top of the tree mould above the surrounding lava surface. Note that this final

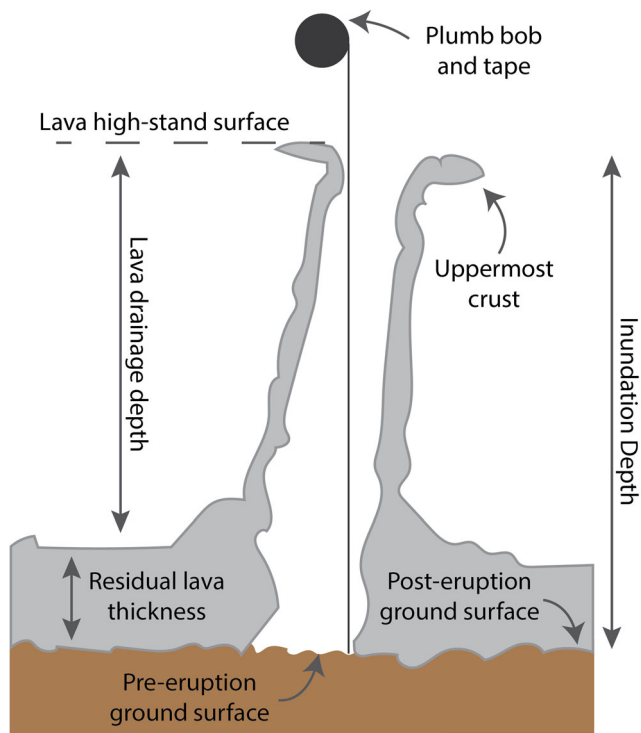


Fig. 2 Schematic tree mould showing the measured features, where the uppermost crust is interpreted to be the lava high-stand surface. The distance from the top of the tree mould to the pre-eruption ground surface—i.e. the inundation depth—was measured using a plumb-bob, dropped down the inside of the mould. The position of the lava high-stand surface and post-eruption ground surface was measured using kinematic GPS. Other quantities were determined by difference

measurement is the same as the difference between measurements 2 and 3 and is therefore redundant in some locations. Measurements are summarized in Fig. 2. We note that a tree mould's internal depth is subject to error if debris has fallen down the cast; therefore, measurements are only reported where a soil horizon was hit by the plumb bob. In the field, the soil horizon was identified by visual inspection if the tree mould was shallow, and if deep, either from the sound heard upon contact or from the presence of soil on the plumb bob. Estimated accuracy of the tree mould depth measurement is ± 2 cm. The location of a specific point within the field area was re-measured seven times using our standard kGPS protocol, enabling quantification of uncertainty in the measured position associated with data acquisition and processing. We obtained a standard deviation of 0.012, 0.017 and 0.018 m, for the E–W, N–S and vertical positions, respectively.

Map production

A geo-referenced database relating all attributes (tree mould height and depth) to their associated kGPS location was created. These data were then imported into a geographic information systems program (ArcGIS™) for all further analysis. Interpolation to produce a raster map was performed using

the tension spline interpolation routine. This routine bends a surface through the known input data points whilst trying to minimize the total curvature of the surface. In a *tension* spline, both first and second derivative terms are used to minimize the curvature of the surface (Franke 1982; Mitáš and Mitášová 1988). We used the routine with 10 points per region and $\phi = 1$, where ϕ is the weight given to the first derivative term and can be thought of as the 'surface stiffness' (Franke 1982). This approach was used to create topographic maps for (1) the pre-eruption ground surface, (2) the lava high-stand surface and (3) the post-eruption ground surface. These maps were produced from the following data (Fig. 2): (1) the kGPS positions of the uppermost crust minus the measured tree mould depth, (2) the kGPS positions of the uppermost crust and (3) the kGPS positions of the post-eruption ground surface respectively.

The three topographic surface maps were used to create two further maps: (1) a map of lava inundation depth during eruption and (2) a map of lava drainage depth. The map of lava inundation was created by subtracting the pre-eruption ground surface raster map from the lava high-stand surface raster map using the ArcMap™ 3D Analyst minus tool. The map of lava drainage depth was created by subtracting the post-eruption ground surface raster map from the lava high-stand surface raster map. We note that it is possible that lava may have compacted slightly post-emplacement. Because our data do not allow us to quantify this process, it must be considered as a potential source of additional uncertainty on lava drainage. Note that, for completeness, we also produce a map of residual lava thickness, presented as Fig. S2 in the supplementary information, by subtracting the pre-eruption ground surface raster map from the post-eruption surface raster map. The distribution of residual lava thickness is not discussed further in this work.

Profile production

One of the goals of our study is to investigate how measured parameters, such as inundation depth, vary along the fissure. This is complicated by the fact that the fissure is discontinuous, and is divided into roughly parallel-trending segments that are offset from one another perpendicular to strike. To create a continuous profile along the entire length of the fissure system, we project each segment of the fissure onto a single line with the same overall trend as the fissure system, where the overall trend line is taken as the line connecting the locations of the western-most and eastern-most fissure exposures. The process is illustrated in Fig. 3. As part of the process, we first geo-referenced the aerial photograph taken by Sandia Labs (Fig. S1) and marked the active fissure segments onto the topographic maps. Next, to link all the discontinuous en echelon segments, we determined the overall trend line for the system, which has bearing 079.365° . From the end of each segment, a tie-line was drawn perpendicular to the overall

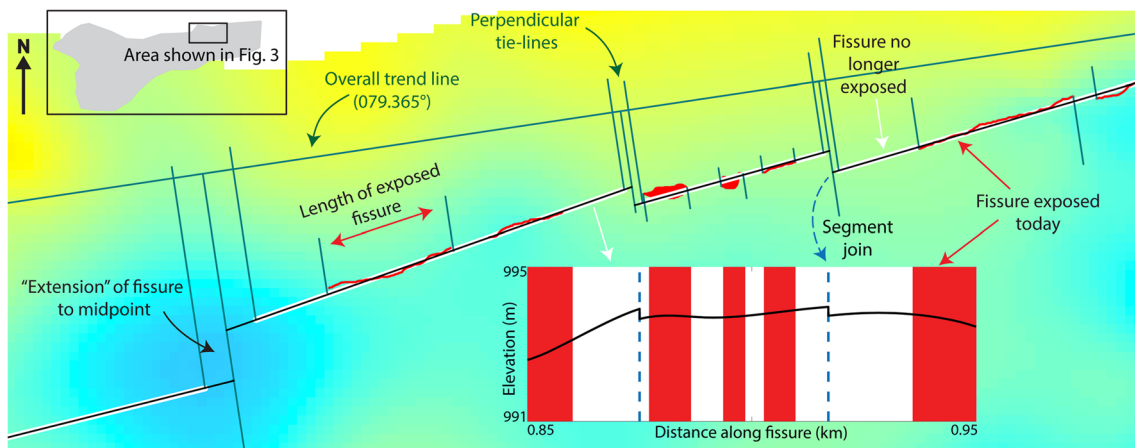


Fig. 3 A labelled portion of the fissure system showing how a continuous profile was constructed from discontinuous fissure segments, using the example of the post-eruption ground surface. The post-eruption ground surface base map used is presented in full in Fig. 4c

trend line, and then the midpoint between the tie-lines, on the overall trend line, was located. Lastly, the segment trend lines were extended within each gap until they met at the midpoint. Parameters were then projected onto the overall trend line to create a continuous profile along strike, allowing us to investigate trends that occur along the entire eruptive fissure.

Results

Topographic maps

Figure 4a shows a map of the pre-eruption ground surface topography prior to the 1969 Mauna Ulu eruption, reconstructed from tree mould depths. Overall, the ground elevation slopes to the south, consistent with the regional trend on the southern flank of the Kīlauea shield. The broad trends in the map are also consistent with the relatively low resolution topographic map (1:24,000 scale; 6.1 m vertical resolution) produced by the US Geological Survey before the 1969 eruption (Plate 1 of Swanson et al. 1979). Note that our absolute elevation values differ from those of Swanson et al. (1979) because we use a different vertical reference datum: Swanson et al. (1979) use a vertical reference of mean sea level whereas we use the WGS 84 reference ellipsoid. In detail, the pre-eruption topography has two broad depressions in the east of the mapped area, starting close to the fissure and sloping southward. Close to the fissure, these depressions are approximately 60 m wide and 1 m deep relative to surrounding topography. Away from the fissure, these depressions broaden to > 170 m and deepen to 4 m. There is a shallow elongate depression, approximately 70 m wide, in the northwest section of the field area. The depression strikes roughly NW–SE and crosses the fissure (but note that there is no exposure of the fissure presently observable in this region). At a smaller scale, below the resolution of this measurement technique, we expect the pre-eruption

ground surface to have had decimetre- and centimetre-scale variations caused by lava surface folding, changes in substrate (e.g. road vs. vegetation) and varying pre-existing lava type (e.g. shelly pāhoehoe vs. ropy pāhoehoe).

The lava high-stand surface (Fig. 4b) also has an overall southward slope. By visual inspection of the contour spacing, this surface in general shows less topographic relief than the pre-eruption ground surface. The northwest region of the field area has the highest elevation (~ 998 m), and there is no clear evidence of the topographic depression observed in the northwest section of the pre-eruption map. The two eastern, south-trending depressions observed in the pre-eruption map can also be detected on this surface, though they are less prominent.

The post-eruption ground surface (i.e. the present day topography; Fig. 4c) is the most robust dataset because it has the highest density of kGPS points (black circles in Fig. 4c); it has been validated through visual comparison with a National Oceanic and Atmospheric Administration digital elevation model (2005 IfSAR DEM). The post-eruption ground surface also has an overall southward slope. In the west, a large, closed basin is present between exposed fissure segments, and in the central and eastern sections, several isolated depressions and topographic highs result in a more variable and steeper relief than that seen in Fig. 4a, b.

Lava inundation

Figure 5 shows the lava inundation depth over the mapped area (i.e. the difference between the lava high-stand and pre-eruption ground surface). Much of the proximal lava flow field was inundated with a 1- to 3-m thickness of lava at peak height. Isolated regions of > 4 m thick lava are commonly associated with depressions in the pre-eruption topography (Fig. 4a).

Also shown in Fig. 5 are segments of the fissure that are in eruption on the Sandia Labs aerial imagery. These segments

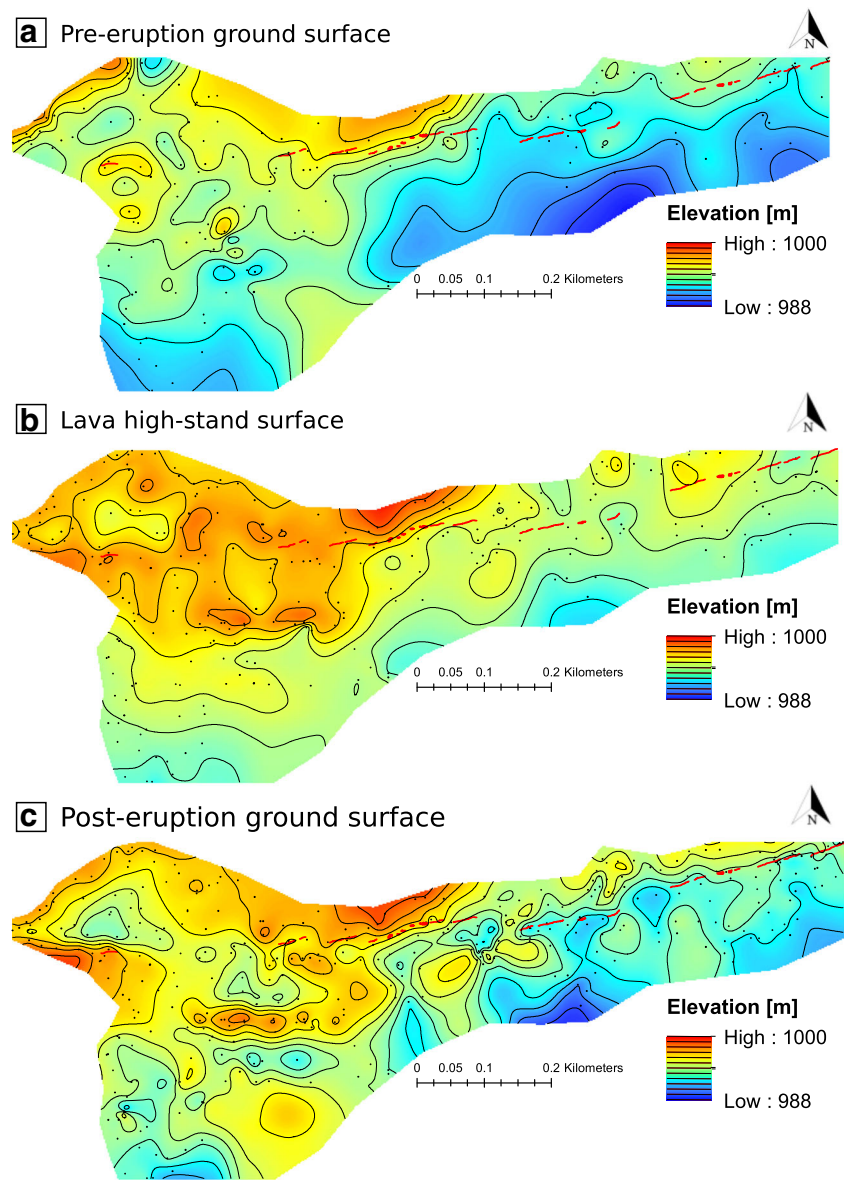


Fig. 4 Topographic maps, contoured at 1 m intervals, of the **a** pre-eruption ground surface topography prior to the 1969 Mauna Ulu eruption, reconstructed from tree mould depths (195 measurements; black dots), **b** lava high-stand surface (269 measurements) and **c** the post-eruption ground surface (383 measurements) produced within ArcMap from kGPS measurements. Not all data points appear in every map,

because some tree moulds were broken and had no high-stand crust, and because measurements of the post-eruption ground surface were not restricted to locations with tree moulds. The fissure vents exposed at the surface today are marked in red. Elevations are ellipsoid heights (WGS 84) and not geoid corrected

appear as orange (incandescent) lines on the images. Segments were traced from the Sandia Labs aerial imagery and overlain onto our maps using Google Earth Pro™. Note that substantial parts of the fissure that were active in the images have no surface expression in the field today. Gaps in exposure of the fissure (Fig. 5) are generally associated with regions of relatively deep lava inundation. This is particularly evident in the western part of the fissure system and at the prominent en echelon step just east of the centre of the fissure system (Fig. 5).

Drainage

Drainage depth varies between 0 and 4 m (Fig. 6). In the western part of the fissure system, drainage is greatest in the basin along fissure segments that once erupted (but are no longer exposed at the surface), removing a maximum of 3.0 m of lava at its centre. In the eastern part of the fissure system, several drainage regions are centred directly along fissure segments and remove a maximum of ~3.5 m of lava. Some of these regions link southward into drainage channels

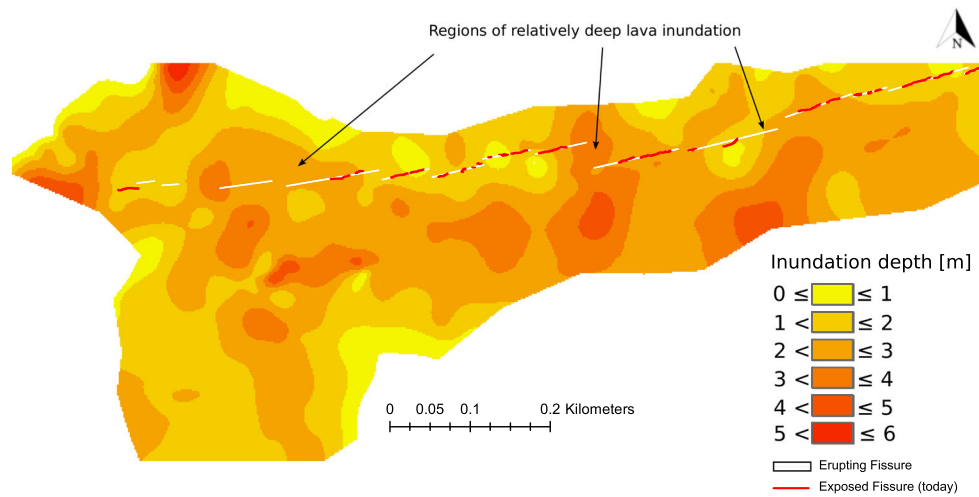


Fig. 5 Map of lava inundation depth during lava high stand. The map is produced by subtracting the pre-eruption ground surface (Fig. 4a) from the lava high-stand surface (Fig. 4b). The fissure vents that can be

observed in the field today are marked in red. Segments of the fissure known to be active during the eruption, identified from the Sandia Labs aerial imagery, are traced in white

(see Fig. 4a, c) and others form closed basins that are similar to, but smaller than, the western basin.

Interpretations

One of our goals is to understand and interpret the lava drainage patterns evidenced by the Mauna Ulu episode 1 field data. We define two terms to describe drainage: ‘outflow’ is the drainage of lava away from the fissure; ‘drain-back’ is the drainage of lava back into the fissure. To set the context for our interpretation of the results previously presented (Figs. 4, 5 and 6), we introduce two hypothetical end-member scenarios. (1) If a region was completely confined, with no pathway for the lava to drain away, then the lava would simply form a pond, and the high-stand surface would be flat and horizontal, with only minor perturbations that correspond to surface ropes

and folding. (2) If all lava could freely drain either down slope, away from the fissure (outflow) or back down the conduit (drain-back), then the lava high-stand surface would reflect only dynamic ponding. These two end-member scenarios, of either widespread ponding or widespread drainage, constitute hypotheses against which we can evaluate the field data.

The situation during episode 1 of the 1969 Mauna Ulu eruption was more complex than these simple end-member scenarios. Whilst the lava high-stand surface in the western part of the fissure system was fairly flat, the eastern part adopted a broad south-sloping trend with smaller scale topographic depressions and highs (Fig. 4b). Additionally, lava inundation depth was not consistent along the fissure (Fig. 5): certain fissure segments, and the adjacent proximal flow field, experienced a deeper inundation above the vent than others. This suggests that, during the eruption, the proximal flow field was characterized by a complex and

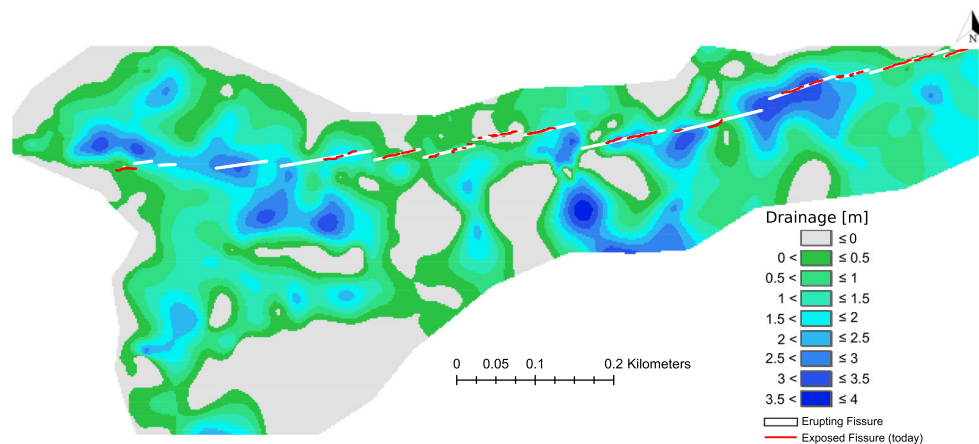


Fig. 6 Map of lava drainage depth. The map is produced by subtracting the post-eruption ground surface (Fig. 4c) from the lava high-stand surface (Fig. 4b). The fissure vents that can be observed in the field

today are marked in red. Segments of the fissure known to be active during the eruption, identified from the Sandia Labs aerial imagery, are traced in white

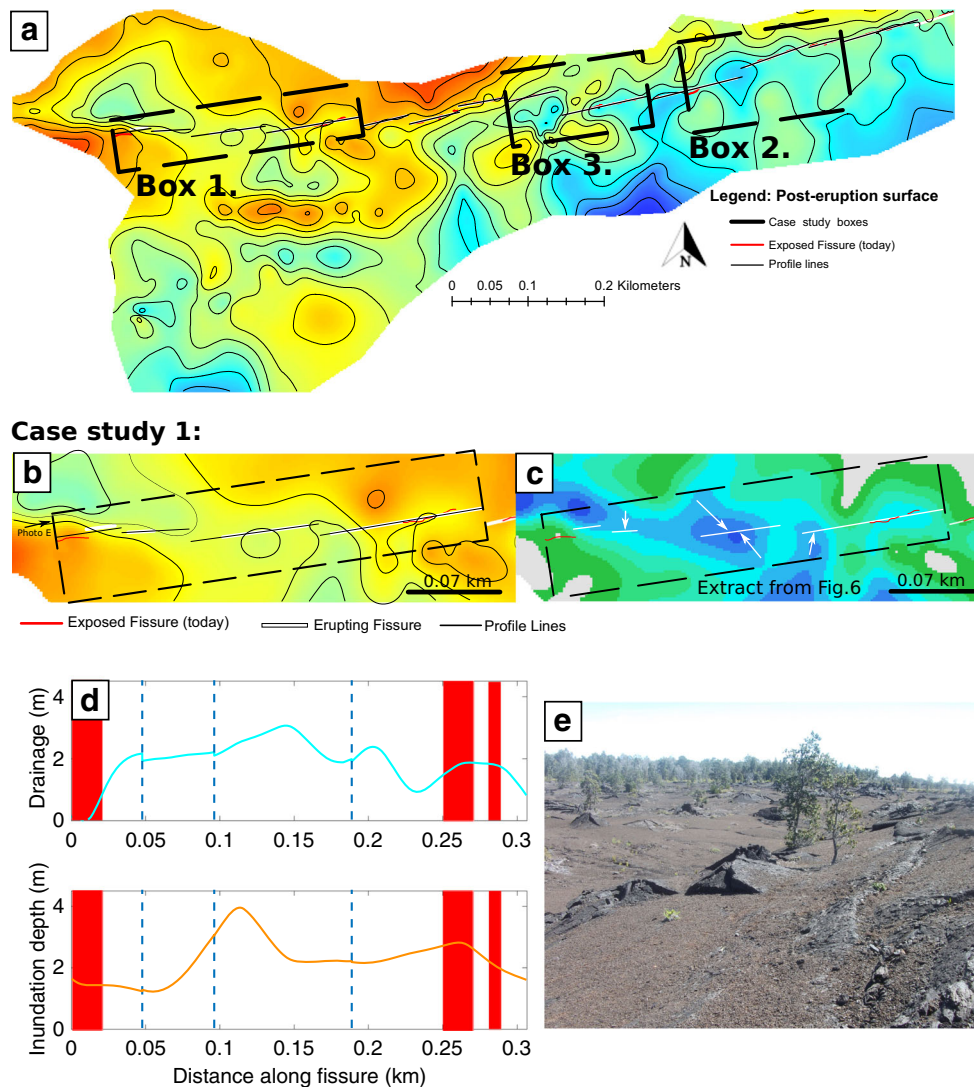


Fig. 7 **a** Post-eruption ground surface (i.e. present day topographic map) highlighting the three case study areas discussed in this study. **b** Detail of the area considered in case study 1 (box 1 in **a**). The red lines show the fissure exposed at the surface today, the white lines show segments of fissure that were active during the eruption and the black lines represent the analysed profiles, constructed according to the methodology presented in the ‘Profile production’ and Fig. 3. **c** An extract from Fig. 5 with arrows showing areas where drainage focused into and around

segments of now-buried fissure. **d** Profiles for drainage (blue) and inundation depth (orange) across box 1. Blue vertical dashed lines represent a step from one fissure segment to another, red-shaded regions mark fissure segments left exposed at the surface today and white regions mark areas where the fissure is no longer exposed. **e** A field photograph of case study 1 (looking east; direction shown by arrow in part **b**) showing the large western basin depression

spatially variable inundation, including elements of both static and dynamic ponding. We explore these complexities in detail by comparing two regions of the proximal flow field. The first region is in the west of the field area (box 1 in Fig. 7a) and has a lava high-stand surface that is relatively flat and horizontal. It contains an unexposed eruptive fissure (Fig. 7b) and forms part of an isolated, closed basin in the pre-eruption topography. The second region is in the east of the field area (box 2 in Fig. 7a) and has a lava high-stand surface that consistently slopes to the south. It includes a prominent south-orientated channel in the pre-eruption topography.

Case study 1: isolated western basin

The first case study location includes four fissure segments (Fig. 7b), all of which erupted material, but which are now either completely covered, with no surface expression, or are only partially exposed. Drainage is at a local maximum on and near the fissure (Fig. 7c). The drainage regions are isolated and do not continue downslope away from the fissure; hence, drainage must have occurred as internal, drain-back into the fissure, along segments that are no longer exposed at the surface. The topographic profile taken from the drainage map along the fissure in box 1 (Fig. 7d)

reveals a maximum of 3 m of drainage (i.e. a 3-m reduction in ground elevation) in the central portion of the fissure, declining in both directions along fissure. The inundation profile along the same portion of the fissure (Fig. 7d) shows that the entire segment had material ponded over the fissure whilst it was erupting. The lava inundation reached a maximum of 3.9 m in the central portion of the fissure and plateaued at ~ 2.2 m to the east. This region of deep lava inundation corresponds to an elongate depression in the pre-eruption topography (Fig. 4a). The inundation depths along the profile are roughly inversely correlated with the palaeo-depression's topography, which has its axis, and therefore deepest inundation, centred ~ 0.12 km from the western end of the fissure.

We infer that, as the episode 1 lava flow field developed, it flooded the isolated western palaeo-depression leading to deep inundation above the erupting fissure. At present, there is a local, isolated depression in this area, indicating that, during the waning stages of the eruption, lava drained back down the fissure (Fig. 7c, e). The amount of drainage varies across the western basin but reaches a maximum between 0.1 and 0.16 km from the western end of the fissure. We hypothesize that this could be because (1) this was the deepest part of the palaeo-depression, where the greatest thickness was available to drain, and/or (2) the depth of the lava allowed it to retain more heat and maintain a lower viscosity than that in the surrounding flow field; hence, it could drain more easily or for longer.

Case study 2: external and internal drainages

For the second case study, we examine an area in the east of the field area, where the Sandia Labs aerial imagery shows lava flows moving south, following pre-existing topographic channels, away from the fissure vent (Fig. 8a and box 2 of Fig. 7a). The drainage map indicates that the drainage depth peaks twice along the fissure (Fig. 8b). Unlike case study 1, there is no correlation between the location of the drainage maxima and the location of areas of deepest lava inundation (Fig. 8b); therefore, we cannot invoke the same drainage mechanisms. To investigate further, we construct two profiles that crosscut the fissure: (1) where it is now covered by lava and hidden (A–A') and (2) where it remains exposed at the surface (B–B'). The pre-eruption ground surface across these two profile lines has a different slope (Fig. 8c): profile A–A' has a shallower proximal gradient than profile B–B'. We infer that, during the eruption, lava was more effectively drained away from the vent-proximal region at fissure location B–B' because of the greater slope. In this area, lava drainage mainly occurred downslope away from the fissure (outflow), rather than internally back into the fissure (drain-back). By contrast, the shallower slope at A–A'

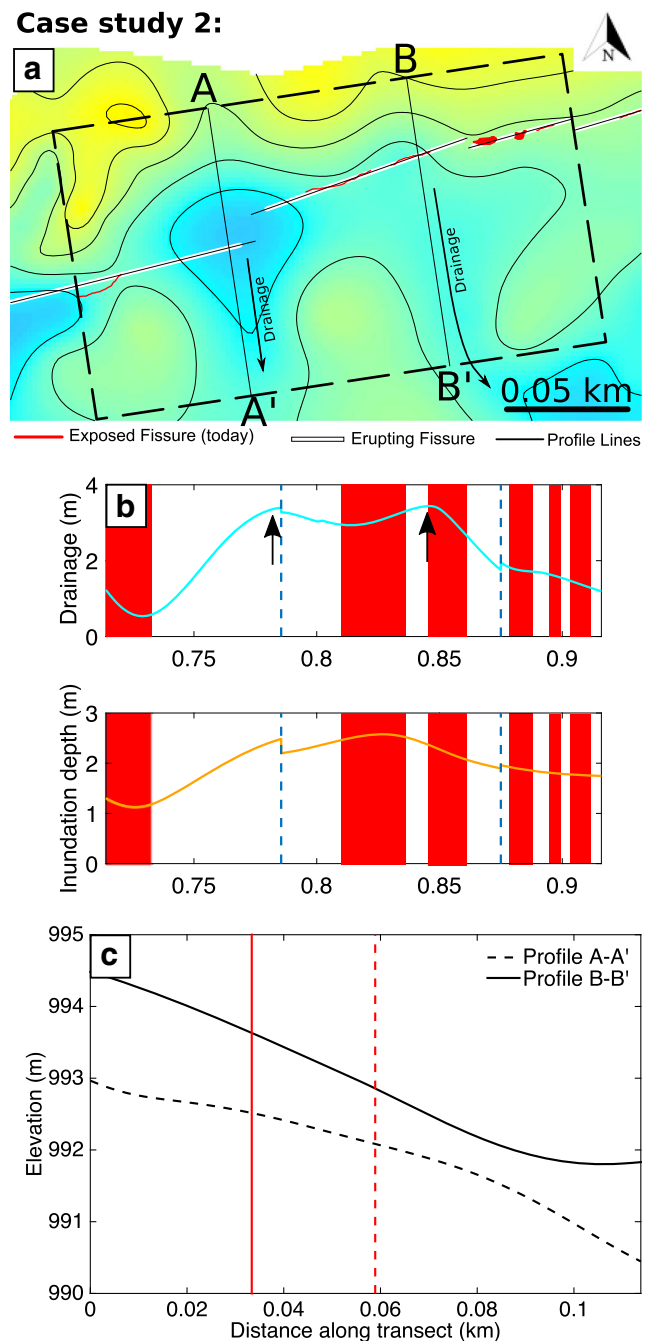


Fig. 8 **a** Detail of the area considered in case study 2 (box 2 in Fig. 7a). The red lines show the fissure exposed at the surface today, the white lines show segments of fissure that were active during the eruption and the black lines represent the analysed profiles. **b** Profiles for drainage (blue) and inundation depth (orange) across box 2; arrows mark two maxima in the drainage profile. **c** Profiles A–A' (dashed) and B–B' (solid) of the pre-eruption ground surface. Vertical red lines mark the intersection between (i) the A–A' profile (dashed red), (ii) the B–B' profile (solid red) and (iii) the fissure

inhibited external, downslope outflow; hence, lava either became dynamically ponded above the vent (when magma supply exceeded outflow) or drained back down fissure.

Discussion

Tree mould mapping provides spatial information on lava drainage that allows us to reconstruct activity at and around missing (buried) fissure segments. The part of the fissure discussed in case study 1 (Fig. 7e) shows no indication of an eruptive vent and has been completely covered by episode 1 lava. Our mapping approach, and the subsequent production of a drainage map, provides a way to constrain the location of the eruptive fissure in the absence of direct observations. It also suggests that calculations of eruptive volume based on the present aerial extent and thickness of deposits are a minimum, because they do not consider erupted material that has drained back down a vent during waning stages.

The two case studies indicate that lava ponded over segments of the fissure either statically, as a result of topographic confinement (case study 1), or dynamically, because magma supply temporarily exceeded outflow (section cut by line A–A', case study 2). In both cases, deep ponding is associated with no exposure of the fissure post-eruption. This suggests that the extent of the lava cover over an erupting vent, in turn a function of pre-eruption topography and the local eruption and outflow fluxes, may influence whether or not it will be preserved post-eruption, with deeply flooded vents less likely to be preserved. To understand the physical rationale for this interpretation, we must consider the effect that ponding has on eruption through an inundated linear vent.

The eruption of spatter through ponded lava was observed directly during the March 2011 Kamoamoia fissure eruption at Kilauea (Lundgren et al. 2013; Orr et al. 2015). In this case, ponding 'drowned' the fissure and locally suppressed eruptive activity (Orr et al. 2015). Slow-moving magma in a fissure loses its heat to the country rock more effectively than fast-flowing magma; hence, its viscosity increases, leading to a positive feedback that promotes stagnation and blocking of the most sluggish portions of a fissure (Bruce and Huppert 1989). This supports a hypothesis that ponding acts to suppress the eruption in that location indirectly by reducing mass flux and causing magma within the underlying section of fissure to slow its ascent. We further contend that fissure eruptions are likely to be particularly susceptible to flow perturbations induced by ponding, because ascending magma can flow laterally to bypass regions of stagnant or down-welling magma more easily than is the case for a circular conduit/vent geometry.

Wilson et al. (1995) present an analysis of the eruption of basaltic magma from a linear fissure vent, through a lava pond, determining the height of lava fountaining as a function of pond depth, exsolved water content and mass eruption rate. They consider only the effect of the additional energy required to eject entrained lava into the fountain and do not consider thermo-rheological effects nor along-fissure migration of flow in response to along-strike variations in pressure gradients.

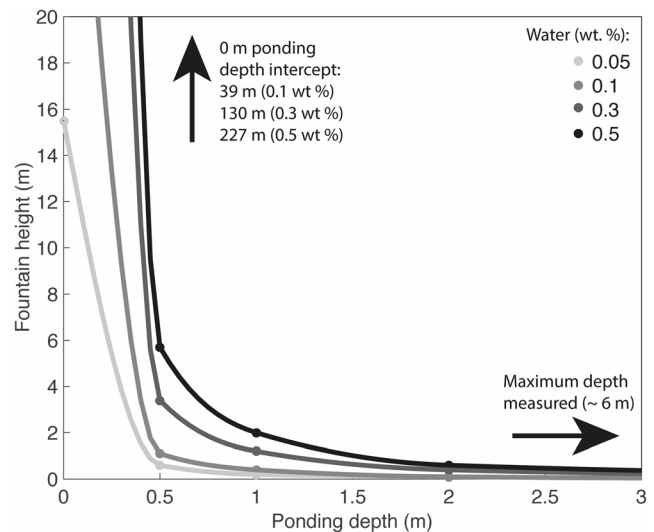


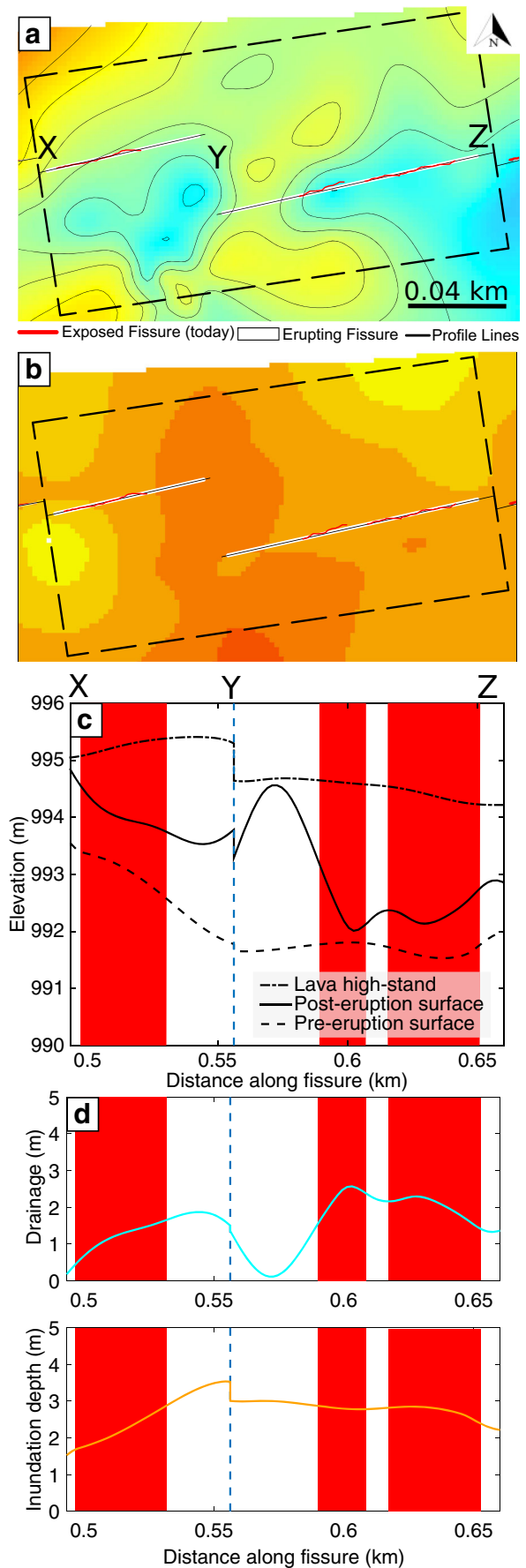
Fig. 9 Fountain height from a linear vent as a function of ponding depth above the vent (data taken from Table 3 of Wilson et al. 1995). The eruption is modelled to have a mass flux of 10^2 kg s^{-1} per meter of fissure with variable exsolved water contents (represented by sequential grey lines). The curves have no physical meaning and are included to guide the eye. For the ponding depths reported in this study (0 to 6 m), it is clear that a dramatic reduction in fountain height would have occurred as ponding depth increased

Nonetheless, an analysis of the episode 1 eruption, following their approach, is instructive. Figure 9 shows estimates of fountain height expected for the eruption as a function of ponding depth, based on data in Table 3 of Wilson et al. (1995). The episode 1 mass eruption rate is estimated from Swanson et al. (1979), who report bulk volumetric eruption rates of $1.30 \times 10^5 \text{ m}^3 \text{ h}^{-1}$ for episode 1 based on the aerial extent and thickness of the lava flows it produced. Using an average lava flow interior bulk density (1750 kg m^{-3}) that we measure from field samples, this equates to an average mass eruption rate of $6.31 \times 10^4 \text{ kg s}^{-1}$. To normalize the mass eruption rate to a unit length of fissure, we measured the length of incandescent fissure (assumed to be erupting) in the Sandia Labs aerial imagery, which were taken approximately 1 h after the fissure system had reached its full length. We found that $\sim 1250 \text{ m}$ of the original 4.5 km fissure was erupting, giving a mass eruption rate per unit length of $50.5 \text{ kg s}^{-1} \text{ m}^{-1}$. This value represents an estimate of the average eruption rate through the whole of episode 1 and neglects temporal variations, for instance during the waxing and waning stages of the eruption; consequently, it should be taken as a minimum estimate of the typical eruption rate when the fissure was at full length. We therefore take $10^2 \text{ kg s}^{-1} \text{ m}^{-1}$ as an order of magnitude estimate for comparison with the model curves of Wilson et al. (1995). We estimate the water loss to be $\sim 0.4 \text{ wt}\%$, calculated as the difference between the assumed water content of basaltic melt at Kilauea's shallow (1–3 km) summit reservoir (0.5 wt%; Moore 1970) and the

water content of spatter from low fountains at Mauna Ulu (0.07 wt%; Swanson and Fabbi 1973).

The results show that an increase in lava pond depth over a fissure strongly influences fountain height (Fig. 9). A ponding depth of 0.5 m above the vent reduces the fountain height by approximately two orders of magnitude compared with the pond-free case—from around 150 m to around 5 m. At ponding depths ≥ 2 m, the fountaining height tends to zero. We note, however, that at shallow ponding depths (≤ 0.3 m), the absolute heights of the lava fountains calculated using the Wilson et al. (1995) approach are much greater than indicated by contemporary field observations. Swanson et al. (1979) report observed maximum fountain heights of 50 m, whilst Parcheta et al. (2012) inferred that fountain heights ranged between 13 and 32 m, based on calibration of field photographs taken at the time of the eruption. One interpretation of the discrepancy between the theoretical calculations and the visual accounts is that all the vents were inundated to some degree. Another possibility is that this discrepancy arises because the model calculations do not account for lateral migration of magma along strike. If flow were to focus laterally, the mass eruption rate would increase at the localization points, resulting in higher fountaining. An increase in ponding depth at one location might therefore lead to an increase in mass eruption rate (and increasing fountain height) in adjacent parts of the fissure.

Our contention that magma can migrate laterally in response to ponding is supported by analysis of episode 1 rampart material (Parcheta et al. 2012) and visual observations at the time of eruption (Swanson et al. 1979), which indicate that fountaining intensity varied laterally along strike and temporally throughout the eruption. For instance, at a single time, variations of 10–15 m in fountain height were observed over short (4–15 m) distances along strike (Swanson et al. 1979; Parcheta et al. 2012). These variations are a result of the progressive vent localization process. To illustrate the effect that variable inundation can have on vent localization, we consider a third case study region within the central portion of the field area (box 3; Fig. 7a). Here, there are vents on two segments of fissure (X–Y and Y–Z) that initially erupted along their entire lateral extent (interpreted from Sandia Labs aerial imagery; Fig. S1) but are today only preserved in limited sections (Fig. 10a). An extract from our lava inundation map (Fig. 10b) shows that the maximum thickness of lava above the vent is highly variable along strike. In this area, the pre-eruption ground surface reaches a local minimum between the two fissure segments (Fig. 10c). The lava inundation profile across the region of interest (Fig. 10a) shows that ponding depth varies between 0.5 and 3.5 m and reaches a maximum in the centre where the fissure is no longer exposed at the surface. This ponding depth range (0.5–3.5 m) is sufficient to result in a large reduction in fountain height (Wilson et al. 1995). We suggest that deeper regions of lava ponding caused



◀ **Fig. 10** **a** Detail of the area considered in case study 3 (box 3 in Fig. 7a). The red lines show the fissure exposed at the surface today, the white lines show segments of fissure that were active during the eruption and the black lines represent the analysed profiles. **b** Lava inundation map of the same area in box 3. The colour scale is the same as for Fig. 4, hotter colours representing greater lava inundation depths (5 m maximum, 0 m minimum in inset). **c** Elevation profiles of the lava high-stand surface and pre-eruption and post-eruption ground surfaces. **d** Profiles for drainage (blue) and inundation depth (orange) across box 3

by palaeo-topography at the east of fissure X–Y, and the west of fissure Y–Z suppressed fountaining in these regions, leading to blocking of the shallow conduit. This is consistent with the observation that the vents are no longer visible and are covered by 1969 lava. It is also possible that proximity to the end of the fissure segments in this region contributed to blocking of the conduit in this region.

Our observations and interpretations support the idea that ponding over the vent may influence local eruption intensity and the longevity of an eruptive segment. In this model, summarized in Fig. 11, suppression of fountaining by deep ponding is followed by stagnation of the eruption at that location and/or drain-back of erupted lava into the conduit. In either case, the viscosity of the magma in that part of the conduit increases, resulting in early shutdown of the eruption at that fissure segment and decreasing the likelihood of it being preserved as an open vent post-eruption. As a corollary, the location of pre-eruption topographic highs intersected by the eruptive fissure appears to correspond with preserved eruptive vents. These palaeo-topographic highs, along fissure from palaeo-lows, have relatively shallow lava ponding depths and are often associated with sub-circular vent geometries. We infer that these parts of the fissure became focal points for ongoing magma ascent and discharge and that consequent mechanical erosion transformed the fissure to a more

circular geometry (Delaney and Pollard 1981; Wylie et al. 1999; Mitchell 2005).

We note that the topographic variation across the Mauna Ulu field site is fairly modest. The pre-eruption ground surface elevation varies along the eruptive fissure by just a few metres (Fig. 4). Furthermore, the mass eruption rates are low ($\sim 50 \text{ kg s}^{-1} \text{ m}^{-1}$). Eruptions with more extreme ($\sim 100 \text{ m}$) topographic variations and much higher mass eruption rates may experience different controls on localization to those discussed in this study.

Conclusions

Tree mould mapping allows the reconstruction of topographic maps for the ground/lava surface before, during and after an eruption. These data can be combined to estimate (1) the depth of lava inundation above the eruptive vent and (2) the amount of drainage that occurred since the lava high-stand. This is particularly useful where syn-eruptive observations are limited or non-existent. We use this technique to investigate the episode 1 fissure system of the 1969 Mauna Ulu eruption of Kīlauea, Hawai‘i, and analyse its evolution from laterally continuous Hawaiian fountaining to more discrete vents, as fissure segments narrowed and closed. Pre-eruption topography is an important control on the evolution of this eruption (Fig. 11): we have shown that the suppression of fountaining by deep ponding—either statically or dynamically—is followed by stagnation of the eruption at that location and/or drain-back of erupted lava into the conduit. In either case, the viscosity of the underlying magma is expected to increase, resulting in early shutdown of the eruption at that fissure segment and decreasing the likelihood of it being preserved as an open vent post-eruption. In contrast, we have shown that parts

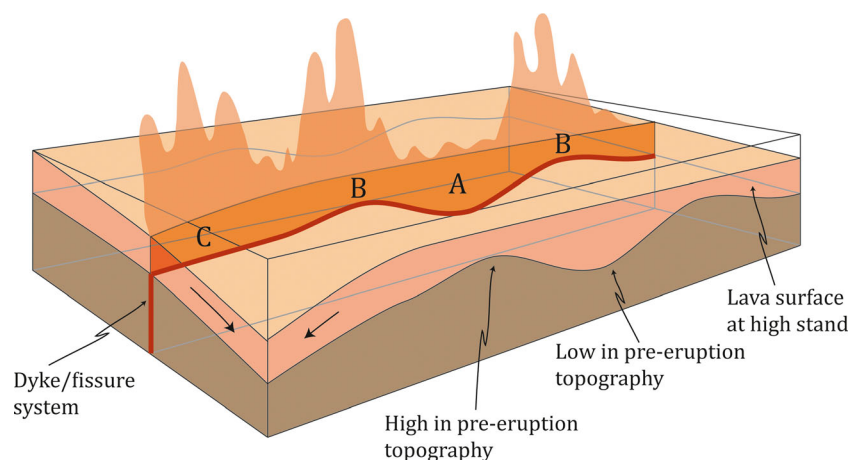


Fig. 11 A simplified schematic of the interaction between the surface and sub-surface processes operating during a fissure eruption. In areas where there was a pre-eruption topographic low (A), the lava is able to inundate and cause deep ponding over the vent. Ponding suppresses the sub-surface

upwelling flux and focuses flow along strike to areas of shallow inundation; these are palaeo-topographic high points (B) and regions with good external drainage/outflow (C). These localization regions are often preserved as open ‘vents’ post-eruption

of the fissure with shallow ponding, such as palaeo-highs and regions where external drainage (outflow) is effective (Fig. 11), are the focal points of continued magma discharge and eruption. We therefore conclude that, in addition to thermal-rheological controls, surface effects (lava inundation, pre-eruption topography, and drainage) can play an important role in the evolution of a basaltic fissure system. Finally, we propose that using the pre-eruption surface to predict the amount of internal (drain-back) and external (outflow) drainage could be a useful tool in hazard forecasting and assessment. For instance, knowing the relative proportion of drain-back and outflow along a fissure could support prediction of the variation in eruption longevity at specific locations along strike, allowing the vent localization pattern to be predicted. Prediction of, or early identification of, those parts of a fissure along which outflow localizes could, in turn, inform source parameters for consequent lava flow hazard modelling.

Acknowledgements Mike Poland is thanked for his support with the kGPS measurements and data processing. Tim Orr and Carolyn Parcheta are thanked for their discussions from which this work benefitted. CVB publishes with the permission of the Executive Director of the British Geological Survey. We thank Matt Patrick, Greg Valentine, the handling editor Jacopo Taddeucci and the executive editor Andrew Harris for their comments that improved the manuscript.

Funding information TJJ is funded by NERC grant NE/L0025901, part of the IAPETUS doctoral training partnership. EWL acknowledges support from NERC grant NE/N018443/1.

Open Access This article is distributed under the terms of the Creative Commons Attribution 4.0 International License (<http://creativecommons.org/licenses/by/4.0/>), which permits unrestricted use, distribution, and reproduction in any medium, provided you give appropriate credit to the original author(s) and the source, provide a link to the Creative Commons license, and indicate if changes were made.

References

- Allard P, Baxter P, Halbwachs M, Komorowski J-C (2002) The January 2002 eruption of Nyiragongo volcano (Dem. Repub. Congo) and related hazards: observations and recommendations. Final report of the French-British scientific team: submitted to the Ministry for Foreign Affairs, Paris, France, Foreign Office, London, United Kingdom and respective Embassies in Democratic Republic of Congo and Republic of Rwanda, Paris, p 24
- Aparone S, Andronico D, Lodato L, Sgroi T (2003) Relationship between tremor and volcanic activity during the Southeast Crater eruption on Mount Etna in early 2000. *J Geophys Res Solid Earth*. <https://doi.org/10.1029/2002JB001866>
- Beckett FM, Burton M, Mader HM et al (2014) Conduit convection driving persistent degassing at basaltic volcanoes. *J Volcanol Geotherm Res* 283:19–35
- Beckett FM, Mader HM, Phillips JC et al (2011) An experimental study of low-Reynolds-number exchange flow of two Newtonian fluids in a vertical pipe. *J Fluid Mech* 682:652–670
- Brown RJ, Thordarson T, Self S, Blake S (2015) Disruption of tephra fall deposits caused by lava flows during basaltic eruptions. *Bull Volcanol* 77:90. <https://doi.org/10.1007/s00445-015-0974-3>
- Bruce PM, Huppert HE (1989) Thermal control of basaltic fissure eruptions. *Nature* 342:665–667
- Bruce PM, Huppert HE (1990) Solidification and melting along dykes by the laminar flow of basaltic magma. In: Ryan MP (ed) *Magma transport and storage*. Wiley, Hoboken, pp 87–101
- Delaney PT, Pollard DD (1982) Solidification of basaltic magma during flow in a dike. *Am J Sci* 282:856–885
- Delaney PT, Pollard DD (1981) Deformation of host rocks and flow of magma during growth of minette dikes and breccia-bearing intrusions near Ship Rock, New Mexico. *US Geol Surv Prof Pap* 1202:61
- Finch RH (1931) Lava tree casts and tree molds. *Volc Lett* 316:1–3
- Franke R (1982) Smooth interpolation of scattered data by local thin plate splines. *Comput Math Appl* 8:273–281
- Geshi N, Neri M (2014) Dynamic feeder dyke systems in basaltic volcanoes: the exceptional example of the 1809 Etna eruption (Italy). *Front Earth Sci* 2:13. <https://doi.org/10.3389/feart.2014.00013>
- Gudmundsson A (1987) Tectonics of the Thingvellir fissure swarm, SW Iceland. *J Struct Geol* 9:61–69. [https://doi.org/10.1016/0191-8141\(87\)90044-7](https://doi.org/10.1016/0191-8141(87)90044-7)
- Harris AJL (2008) Modeling lava lake heat loss, rheology, and convection. *Geophys Res Lett*. <https://doi.org/10.1029/2008GL033190>
- Harris AJL, Flynn LP, Rothery DA et al (1999) Mass flux measurements at active lava lakes: implications for magma recycling. *J Geophys Res Solid Earth* 104:7117–7136
- Helfrich KR (1995) Thermo-viscous fingering of flow in a thin gap: a model of magma flow in dikes and fissures. *J Fluid Mech* 305:219–238
- Huppert HE, Hallworth MA (2007) Bi-directional flows in constrained systems. *J Fluid Mech* 578:95–112
- Kazahaya K, Shinohara H, Saito G (1994) Excessive degassing of Izu-Oshima volcano: magma convection in a conduit. *Bull Volcanol* 56:207–216
- Keating GN, Valentine GA, Krier DJ, Perry FV (2008) Shallow plumbing systems for small-volume basaltic volcanoes. *Bull Volcanol* 70:563–582. <https://doi.org/10.1007/s00445-007-0154-1>
- Larsen G (2000) Holocene eruptions within the Katla volcanic system, south Iceland: characteristics and environmental impact. *Jökull* 49:1–28
- Lefebvre NS, White JDL, Kjarsgaard BA (2012) Spatter-dike reveals subterranean magma diversions: consequences for small multivalent basaltic eruptions. *Geology* 40:423–426
- Lockwood JP, Lipman PW (1980) Recovery of datable charcoal beneath young lavas: lessons from Hawaii. *Bull Volcanol* 43:609–615
- Lockwood JP, Williams IS (1978) Lava trees and tree moulds as indicators of lava flow direction. *Geol Mag* 115:69–74
- Lundgren P, Poland M, Miklius A et al (2013) Evolution of dike opening during the March 2011 Kamoamoā fissure eruption, Kīlauea Volcano, Hawai‘i. *J Geophys Res Solid Earth* 118:897–914. <https://doi.org/10.1002/jgrb.50108>
- Mitáš L, Mitášová H (1988) General variational approach to the interpolation problem. *Comput Math Appl* 16:983–992
- Mitchell KL (2005) Coupled conduit flow and shape in explosive volcanic eruptions. *J Volcanol Geotherm Res* 143:187–203
- Moore JG (1970) Water content of basalt erupted on the ocean floor. *Contrib Mineral Petrol* 28:272–279
- Moore JG, Richter DH (1962) Lava tree molds of the September 1961 eruption, Kīlauea Volcano, Hawaii. *Geol Soc Am Bull* 73:1153–1158
- Opheim JA, Gudmundsson A (1989) Formation and geometry of fractures, and related volcanism, of the Krafla fissure swarm, northeast Iceland. *Geol Soc Am Bull* 101:1608–1622. [https://doi.org/10.1130/0016-7606\(1989\)101<1608:FAGOFA>2.3.CO;2](https://doi.org/10.1130/0016-7606(1989)101<1608:FAGOFA>2.3.CO;2)

- Oppenheimer C, Francis P (1997) Remote sensing of heat, lava and fumarole emissions from Erta'Ale volcano, Ethiopia. *Int J Remote Sens* 18:1661–1692
- Oppenheimer C, Kyle PR (2008) Probing the magma plumbing of Erebus volcano, Antarctica, by open-path FTIR spectroscopy of gas emissions. *J Volcanol Geotherm Res* 177:743–754
- Orr TR, Poland MP, Patrick MR et al (2015) Kilauea's 5–9 March 2011 Kamoamoao fissure eruption and its relation to 30+ years of activity from Pu'u "O". In: Carey R, Poland M, Cayol V, Weis D (eds) *Hawaiian volcanism: from source to surface*, American Geophysical Union geophysical monograph, vol 208. Wiley, Hoboken (2015), pp 393–420
- Palma JL, Blake S, Calder ES (2011) Constraints on the rates of degassing and convection in basaltic open-vent volcanoes. *Geochim Geophys Geosyst*. <https://doi.org/10.1029/2011GC003715>
- Parcheta C, Fagents S, Swanson DA et al (2015) Hawaiian fissure fountains: quantifying vent and shallow conduit geometry, Episode 1 of the 1969–1974 Mauna Ulu Eruption. In: Carey R, Poland M, Cayol V, Weis D (eds) *Hawaiian volcanism: from source to surface*, American Geophysical Union geophysical monograph, vol 208. Wiley, Hoboken (2015), pp 369–391
- Parcheta CE, Houghton BF, Swanson DA (2012) Hawaiian fissure fountains 1: decoding deposits—episode 1 of the 1969–1974 Mauna Ulu eruption. *Bull Volcanol* 74:1729–1743
- Parcheta CE, Pavlov CA, Wiltsie N et al (2016) A robotic approach to mapping post-eruptive volcanic fissure conduits. *J Volcanol Geotherm Res* 320:19–28
- Patrick MR, Anderson KR, Poland MP et al (2015) Lava lake level as a gauge of magma reservoir pressure and eruptive hazard. *Geology* 43:831–834
- Pedersen GBM, Höskuldsson A, Dürig T et al (2017) Lava field evolution and emplacement dynamics of the 2014–2015 basaltic fissure eruption at Holuhraun, Iceland. *J Volcanol Geotherm Res* 340:155–169. <https://doi.org/10.1016/j.jvolgeores.2017.02.027>
- Philpotts AR, Philpotts DE (2007) Upward and downward flow in a camptonite dike as recorded by deformed vesicles and the anisotropy of magnetic susceptibility (AMS). *J Volcanol Geotherm Res* 161:81–94. <https://doi.org/10.1016/j.jvolgeores.2006.11.006>
- Reynolds P, Brown RJ, Thordarson T, Llewellyn EW (2016) The architecture and shallow conduits of Laki-type pyroclastic cones: insights into a basaltic fissure eruption. *Bull Volcanol* 78:1–18. <https://doi.org/10.1007/s00445-016-1029-0>
- Richter DH, Eaton JP, Murata KJ et al (1970) Chronological narrative of the 1959–60 eruption of Kilauea volcano, Hawaii. *US Geol. Surv. Prof. Paper*:537
- Sigurdsson H (2000) Volcanic episodes and rates of volcanism. In: *Encyclopedia of volcanoes*. Academic Press, San Diego, pp 271–279
- Stevenson DS, Blake S (1998) Modelling the dynamics and thermodynamics of volcanic degassing. *Bull Volcanol* 60:307–317
- Stothers RB, Wolff JA, Self S, Rampino MR (1986) Basaltic fissure eruptions, plume heights, and atmospheric aerosols. *Geophys Res Lett* 13:725–728
- Stovall WK, Houghton BF, Harris AJL, Swanson DA (2009) Features of lava lake filling and draining and their implications for eruption dynamics. *Bull Volcanol* 71:767–780
- Sumner JM, Blake S, Matela RJ, Wolff JA (2005) Spatter. *J Volcanol Geotherm Res* 142:49–65
- Swanson DA, Duffield WA, Jackson DB et al (1979) Chronological narrative of the 1969–71 Mauna Ulu eruption of Kilauea Volcano. *Hawaii US Geol Surv Prof Paper*:1056
- Swanson DA, Fabbi BP (1973) Loss of volatiles during fountaining and flowage of basaltic lava at Kilauea volcano, Hawaii. *J Res US Geol Surv* 1:649–658
- Thorarinsson S, Steinthorsson S, Einarsson T et al (1973) The eruption on Heimaey, Iceland. *Nature* 241:372–375
- Thordarson T, Self S (1993) The Laki (Skaftár Fires) and Grimsvötn eruptions in 1783–1785. *Bull Volcanol* 55:233–263
- Tilling R, Christian R, Duffield WA et al (1987) The 1972–1974 Mauna Ulu eruption, Kilauea Volcano: an example of quasi steady-state magma transfer. *US Geol Surv Prof Pap* 1350:405–469
- Tilling RI (1987) Fluctuations in surface height of active lava lakes during 1972–1974 Mauna Ulu eruption, Kilauea volcano, Hawaii. *J Geophys Res Solid Earth* 92:13721–13730
- Valentine GA, Gregg TKP (2008) Continental basaltic volcanoes—processes and problems. *J Volcanol Geotherm Res* 177:857–873
- Wadsworth FB, Kennedy BM, Branney MJ et al (2015) Exhumed conduit records magma ascent and drain-back during a Strombolian eruption at Tongariro volcano, New Zealand. *Bull Volcanol* 77:1–10. <https://doi.org/10.1007/s00445-015-0962-7>
- Walker GPL, Self S, Wilson L (1984) Tarawera 1886, New Zealand a basaltic plinian fissure eruption. *J Volcanol Geotherm Res* 21:61–78
- Whitehead JA, Helfrich KR (1991) Instability of flow with temperature-dependent viscosity: a model of magma dynamics. *J Geophys Res Solid Earth* 96:4145–4155. <https://doi.org/10.1029/90JB02342>
- Wilson L, Parfitt EA, Head JW (1995) Explosive volcanic eruptions—VIII. The role of magma recycling in controlling the behaviour of Hawaiian-style lava fountains. *Geophys J Int* 121:215–225. <https://doi.org/10.1111/j.1365-246X.1995.tb03522.x>
- Witham F, Llewellyn EW (2006) Stability of lava lakes. *J Volcanol Geotherm Res* 158:321–332
- Wolfe EW (ed) (1988) *The Puu Oo eruption of Kilauea Volcano, Hawaii: episodes 1 through 20, January 3, 1983 through June 8, 1984*. US Geol Surv Prof Pap 1463:251
- Woods AW (1993) A model of the plumes above basaltic fissure eruptions. *Geophys Res Lett* 20:1115–1118
- Wright TL, Kinoshita WT, Peck DL (1968) March 1965 eruption of Kilauea volcano and the formation of Makaopuhi lava lake. *J Geophys Res* 73:3181–3205
- Wunderman R (2002) Report on Nyiragongo (DR Congo). *Bull Glob Volcanism Netw*. <https://doi.org/10.5479/si.GVP.BGVN200204-223030>
- Wylie JJ, Helfrich KR, Dade B et al (1999) Flow localization in fissure eruptions. *Bull Volcanol* 60:432–440. <https://doi.org/10.1007/s004450050243>
- Wylie JJ, Lister JR (1995) The effects of temperature-dependent viscosity on flow in a cooled channel with application to basaltic fissure eruptions. *J Fluid Mech* 305:239–261